Cell
PRESS

Movies of Ice-Embedded Particles Enhance Resolution in Electron Cryo-Microscopy

Melody G. Campbell,[1,5] Anchi Cheng,[1,5] Axel F. Brilot,[4] Arne Moeller,[1] Dmitry Lyumkis,[1] David Veesler,[1] Junhua Pan,[2] Stephen C. Harrison,[2,3] Clinton S. Potter,[1] Bridget Carragher,[1] and Nikolaus Grigorieff[3,4,*]
[1]National Resource for Automated Molecular Microscopy, Department of Cell Biology, The Scripps Research Institute, La Jolla, CA 92037, USA
[2]Harvard Medical School and Children's Hospital, Boston, MA 02115, USA
[3]Howard Hughes Medical Institute
[4]Department of Biochemistry, Rosenstiel Basic Medical Sciences Research Center
Brandeis University, MS029, 415 South Street, Waltham, MA 02454, USA
[5]These authors contributed equally to this work
*Correspondence: niko@brandeis.edu
http://dx.doi.org/10.1016/j.str.2012.08.026

SUMMARY

Low-dose images obtained by electron cryo-microscopy (cryo-EM) are often affected by blurring caused by sample motion during electron beam exposure, degrading signal especially at high resolution. We show here that we can align frames of movies, recorded with a direct electron detector during beam exposure of rotavirus double-layered particles, thereby greatly reducing image blurring caused by beam-induced motion and sample stage instabilities. This procedure increases the efficiency of cryo-EM imaging and enhances the resolution obtained in three-dimensional reconstructions of the particle. Using movies in this way is generally applicable to all cryo-EM samples and should also improve the performance of midrange electron microscopes that may have limited mechanical stability and beam coherence.

INTRODUCTION

Electron cryo-microscopy (cryo-EM) has developed over the past 4 decades as a technique for visualizing the three-dimensional (3D) structures of macromolecules and their assemblies. Two-dimensional (2D) crystals provided resolutions of 4 Å or better in the 1990s (e.g., Henderson et al., 1990; Kühlbrandt et al., 1994; Nogales et al., 1998); helical assemblies yielded comparable resolutions about a decade later (e.g., Sachse et al., 2007; Unwin, 2005; Yonekura et al., 2003); and most recently, large icosahedral viruses have done the same (see Grigorieff and Harrison, 2011, for a review). The steady advances in the technique have included better sample preparation methods (e.g., microfabricated grids; Ermantraut et al., 1998; Quispe et al., 2007), better electron microscopes (e.g., field emission guns; Henderson et al., 1990), spot-scan (Bullough and Henderson, 1987), improved image processing algorithms (e.g., MRC image processing package [Crowther et al., 1996], EMAN [Tang et al., 2007], FREALIGN [Grigorieff, 2007], CTFFIND3,

and CTFTILT [Mindell and Grigorieff, 2003]), and more powerful computing systems. Further technological improvements are currently underway, including phase plates to enhance low-resolution contrast (Cambie et al., 2007; Danev and Nagayama, 2001; Majorovits et al., 2007; Muller et al., 2010), direct electron detectors that increase the signal-to-noise ratio (SNR) in the recorded images (McMullan et al., 2009; Milazzo et al., 2005), and new algorithms to accommodate conformational and compositional variability in the imaged sample (Penczek et al., 2011; Scheres et al., 2007).

Among the remaining problems currently limiting the attainable resolution is the motion of the sample that occurs while it is exposed to the high-energy electron beam. In a recent study, we showed that the beam causes particles suspended in a thin layer of vitreous ice inside holes in a perforated carbon support film to shift by up to a few nanometers and rotate by up to a few degrees, causing significant blurring in many of the images (Brilot et al., 2012). As the motion occurs in the ice layer, neighboring particles move in a similar fashion. The blurring due to beam-induced motion (BIM) is likely one of the main reasons why the number of images required to achieve 4 Å resolution or better is significantly larger than predicted by calculations based on the SNR of idealized low-dose images (Glaeser, 1999; Henderson, 1995). We characterized BIM earlier using exposure series and movies obtained using a direct electron detector (Brilot et al., 2012). As we noted, the movies can be used to reduce image blurring caused by BIM and stage instabilities by averaging the movie frames after aligning the individual frames to bring them into register with each other. In the present work, we demonstrate this possibility by comparing reconstructions calculated from movies without frame alignment and reconstructions calculated from movies with frames that have been aligned to correct for sample motion. We show that the movie-frame alignment substantially increases the overall resolution that can be obtained from a relatively small cryo-EM data set.

RESULTS

Movie Processing

We recorded 501 movies of rotavirus double-layered particles (DLPs), the same sample that was used in our previous work
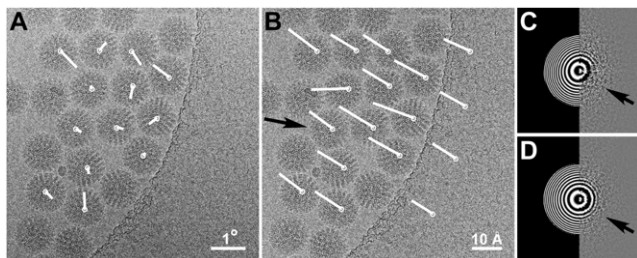
Figure 1. Reduced Image Blurring with Movie Frame Alignment

(A) An example of an image that experienced blurring due to a sample shift of about 10 Å. The white vectors indicate direction and amount of particle rotations measured between the first and last four frames of the recorded 16-frame movie.

(B) The same image as in (A) after frame alignment based on the shifts measured for the DLP highlighted by the arrow. The white vectors indicate direction and amount of particle shifts measured between the first and last four frames of the movie. Additionally, shifts of the carbon support film were measured in four different locations using correlation maps between patches of 512 × 512 pixels of the four-frame averages.

(C) Thon ring pattern (right) calculated from the image in (A) showing loss of contrast (arrow indicates the weaker or missing Thon rings) in one direction due to the sample motion, and fitted pattern (left) using the computer program *CTFFIND3* (Mindell and Grigorieff, 2003). The fit extends to a resolution of 5 Å and corresponds to a defocus of 1.1 μm.

(D) Thon ring pattern and fit after frame alignment; image shown in (B). The extension of the rings is now nearly isotropic (indicated by the arrow).
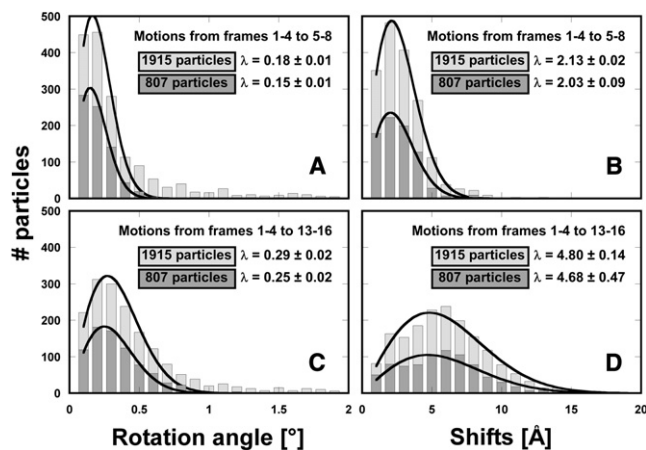

Figure 2. Histograms of the Particle Rotations and Shifts Measured by Motion Tracking Using Movies

There is no significant difference in the distributions of the whole data set (1,915 particles, light gray) and the best 42% of the data (807 particles, dark gray). Particle motions are measured between averages of frames 1–4 and 5–8 in (A) and (B) and between 1–4 and 13–16 in (C) and (D). Each distribution is fitted with a Rayleigh distribution to determine its maximum λ (the median motion value). Standard errors are indicated for each fit.

(Brilot et al., 2012). These particles previously yielded an ∼4 Å reconstruction using data recorded on photographic film (Zhang et al., 2008) (referred to here as "the 2008 data set"). To track particle motion during beam exposure, we recorded movies consisting of 16 frames during continuous electron exposure (see Experimental Procedures). To track sample motion, we followed our previous procedure (Brilot et al., 2012) and generated averages of four movie frames at a time, corresponding to an electron dose of about eight electrons/Å^2 in each average, providing sufficient signal to align images of individual particles against a reference reconstruction of the DLP (Zhang et al., 2008). The tracking showed temporal dependence of the motion similar to what we saw previously, with faster initial motion that slowed toward the end of the exposure (Brilot et al., 2012). We used the particle coordinates and Euler angles measured in the four-frame averages as time points to describe particle trajectories and derived particle parameters for individual movie frames from fits to a quadratic function for each particle trajectory.

Correcting Beam-Induced Motion and Sample Drift

Figure 1 shows an area of sample that experienced a shift of about 10 Å during the exposure. The average calculated without alignment from all 16 frames is shown in Figure 1A. There is evidence of significant blurring and loss of detail in the Thon ring pattern (Thon, 1966) calculated for this frame average (Figure 1C). After shift alignment of the frames to compensate for sample drift and BIM (Figure 1B), the Thon ring pattern (Figure 1D) appears more uniform, indicating near-isotropic resolution.

We obtained a total of 1,915 particles from the movies and selected the best ∼40% (807 particles) for 3D reconstruction,

based on their correlation coefficients with a reference reconstruction. We chose the percentage of included particles to correspond to the percentage used in the final reconstructions from the 2008 data set, which we used as a reference to evaluate the quality of the movie data (discussed later). Figure 2 shows a histogram of the measured rotations and shifts that occurred between averages of the first and second groups of four movie frames (Frames 1–4 and 5–8, respectively) and between averages of the first and last group of four movie frames (Frames 1–4 and 13–16, respectively). The motions occurring between the first and second group of movie frames is directly comparable with our earlier experiments in which we analyzed the motions between single exposures of 8 electrons/Å^2 (Brilot et al., 2012). Each histogram is fitted with a Rayleigh distribution to obtain the median value λ (Brilot et al., 2012). Separate histograms are shown for the full data set and the 807 particles selected for 3D reconstruction, showing that there is no significant difference in the distributions of observed rotations and shifts.

Between averages of the first and second groups of four movie frames, measured rotations range from a fraction of a degree to a few degrees with a distribution maximum at about 0.2° (Figure 2A). This is substantially smaller than the previously observed 0.44° (Brilot et al., 2012) for a similar dose rate (80 electrons/Å^2/s). In our previous analysis, we estimated the angular alignment accuracy to be about 0.2°, close to the majority of rotations plotted in Figure 2A. The distribution of rotations is therefore broadened by an alignment error and actual rotations are likely smaller than suggested by the histogram in Figure 2A. Shifts range from a fraction of an angstrom to over 20 Å, with a distribution maximum at about 2 Å (Figure 2B). Larger motions were measured between averages of the first and last groups of four frames, with distribution maxima at about 0.3° (Figure 2C) and about 5 Å for rotations and shifts, respectively. The broadening

of the histogram of rotations may in part be the result of somewhat increased alignment errors due to degraded signal in the final four-frame average, which shows increased radiation damage compared with the earlier frame averages. Figure 1A shows an example of measured particle rotations within a movie. The measured angles are relatively small, and their directions are uncorrelated, consistent with these measurements being at the limit of our alignment accuracy.

The observed shifts are likely a combination of BIM and stage drift, which are difficult to distinguish in our experiments. However, as part of the Leginon recording cycle, drift rates were measured each time the stage was moved to a different area of the grid (translations larger than 10 μm). Following 96% of these translational movements, an average drift rate of 1.6 Å/s (SD = 0.7 Å/s) was achieved after 20 s. A much smaller translation (less than 2 μm) was subsequently used to move to the area where movies were recorded. Although no further monitoring of the stage drift was performed after these smaller translations, it is reasonable to assume that the average drift rate did not change significantly. Assuming a drift rate of 1.6 Å/s, the sample moved only by about 1 Å during the course of the movies (0.6 s). The measured shifts plotted in Figure 2D can therefore mainly be attributed to BIM. Nevertheless, it should be noted that our motion tracking procedure does not depend on the source of the measured shifts, and blurring due to both stage drift and BIM will be corrected.

Improved 3D Reconstructions

A particle moving by about 5 Å will have a standard deviation from its average position of about 1.5 Å, producing a temperature factor (B-factor) of about 200 Å^2 (Jensen, 2001). Without motion tracking, the majority of particles experience shifts larger than 5 Å during the entire length of the movies (Figure 2D) and will contribute with an even higher effective temperature factor. Rotations of 0.3° will add an average B-factor of 160 Å^2 (Jensen, 2001), giving a total B-factor of about 360 Å^2 due to motion. Using our motion tracking procedure to reduce blurring in the particle images, we calculated icosahedrally symmetrized reconstructions of DLP. As expected, the B-factors of these reconstructions were significantly reduced, by about 160 Å^2, relative to the reconstructions that were not motion compensated (Figure 3A). Figure 3B shows Fourier shell correlation (FSC) curves for the DLP reconstruction, and for the rotavirus VP6 coat protein after additional 13-fold nonicosahedral averaging (Zhang et al., 2008), calculated without motion tracking, with motion tracking that accounts only for particle shifts, and with motion tracking that accounts for shifts and rotations. The curves indicate significant improvements in the resolution in both DLP and VP6 densities when compensating for shifts, and further minor improvements when including rotations. The resolution of the DLP reconstruction improved from 7.5 Å to 6.4 Å and 6.2 Å, respectively, while that of the averaged VP6 reconstruction improved from 4.9 Å to 4.4 Å and 4.4 Å, respectively (at FSC = 0.143; Rosenthal and Henderson, 2003). The improvement agrees with the observed B-factor reduction of 160 Å^2, which is equivalent to an 8-fold structure factor increase at 4.4 Å. This 8-fold increase translates into a 60-fold reduction of the number of particles required to achieve the same signal without amplification.
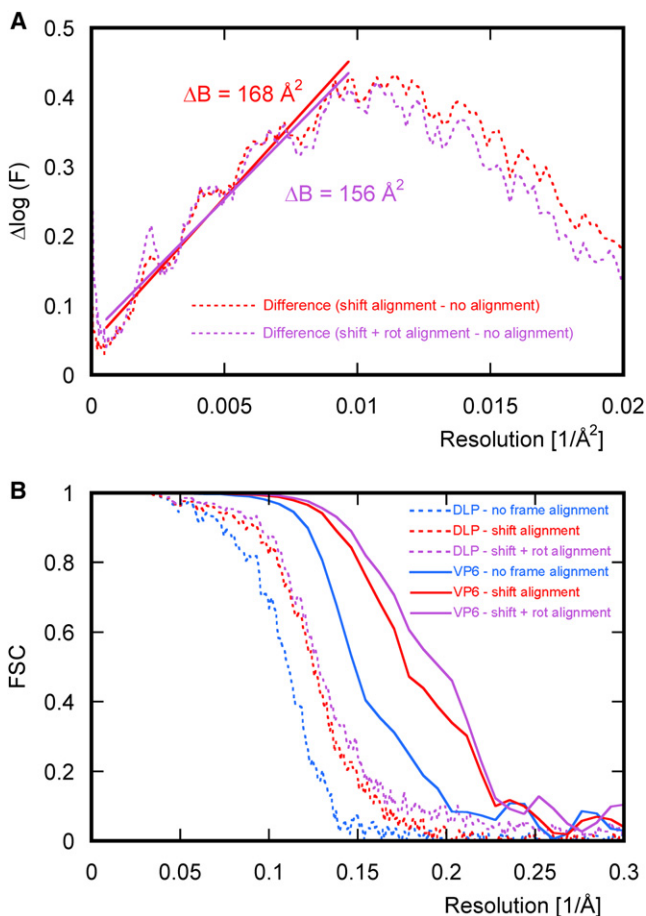

Figure 3. Improvement in Resolution with Frame Alignment

(A) The difference between the natural logarithm of the average structure factors F (dotted lines) of DLP reconstructions obtained with and without frame alignment, as a function of squared reciprocal resolution. The plots allow estimation by a linear fit of the B-factor reduction obtained with shift alignment (red line) and additional rotational alignment (purple line).

(B) FSC curves for reconstructions of icosahedrally averaged reconstructions of DLP and rotavirus VP6 coat protein after additional 13-fold nonicosahedral averaging, calculated using data from all 16 movie frames. The dotted and solid lines correspond to DLP and VP6 reconstructions, respectively, while blue, red, and purple correspond to reconstructions obtained without frame alignment, with shift alignment, and with both shift and rotational alignment, respectively.

In Figure 4, we compare details that can be seen in the 13-fold averaged VP6 density calculated with and without motion tracking, to similar details seen in the 2008 reconstruction (Zhang et al., 2008). We fit densities with an atomic model of VP6 obtained by X-ray crystallography (Protein Data Bank [PDB] ID: 3KZ4; McClain et al., 2010) to help the interpretation. All maps show density corresponding to amino acid side chains. Compared to the density calculated without motion tracking (Figure 4A), the reconstruction that takes sample shifts into account improves substantially, and the density for many of the larger side chains is significantly stronger (Figure 4B). Taking into account both shifts and rotations leads to a map with further minor improvements (Figure 4C), as expected (discussed earlier). The improved detail in the densities shown in
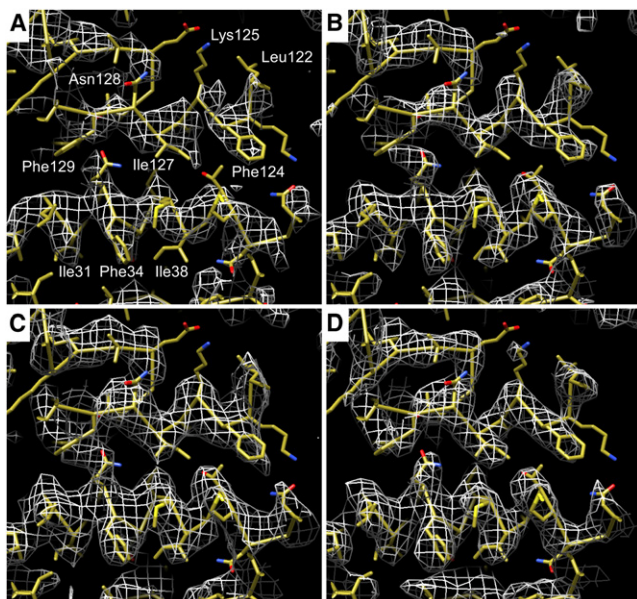
Figure 4. Comparison of Density Maps

(A) α-helical region of the VP6 density calculated using images derived from movies by simple frame averaging without motion tracking. Density for some of the larger amino acid side chains is visible.

(B) Same as in (A) but with shift alignment of the movie frames to reduce blurring in the images. The side chain density is significantly stronger compared to (A).

(C) Same as in (A) but with additional rotational alignment of the movie frames taken into account during 3D reconstruction.

(D) Same as in (A) for the map published in 2008 (EMDB 1461). The crystal structure of VP6 (PDB ID: 3KZ4; McClain et al., 2010) is superimposed on the density in (A) through (D) to aid interpretation of the features. For accurate comparison, the maps in (A), (B), and (C) were scaled to match the rotationally averaged amplitude spectrum of the map in (D) and contoured at the same density threshold as in (D) using *UCSF Chimera* (Goddard et al., 2007).

Figures 4B and 4C are also indicated by the increase in the FSC calculated for the reconstructions (Figure 3B), showing a resolution increase from 4.9 Å (without motion tracking) to 4.4 Å (with motion tracking). Comparison of the motion-compensated map with the map obtained in 2008 (Figure 4D), which was calculated using 10 times as many particle images to yield a resolution of 4.1 Å (FSC = 0.143), suggests that the two maps are of similar quality.

DISCUSSION

One of the main problems limiting the resolution attainable in cryo-EM reconstructions of ordered arrays, such as 2D crystals and helical assemblies, and of single particles, such as viruses and ribosomes, is BIM, which causes blurring in the recorded images. We have shown here that blurring due to BIM and stage drift can be reduced by recording movies of the sample as it is exposed to the electron beam, followed by alignment of individual movie frames (Figure 1). The reduced blurring leads to a substantial improvement in resolution (Figure 3) and map quality. Achieving the resolution of the final 13-fold averaged density in Figure 4B (4.4 Å) required a total of approximately 630,000 (i.e., 807 × 60 × 13) VP6 subunits, while it took 6.6 million

subunits to obtain a resolution of 4.1 Å with the 2008 data set, and both maps are of similar quality. The 10-fold reduction of required data arises partly due to the compensation for sample motion, but the observed decrease in B-factor by 160 Å^2 would indicate a 60-fold reduction in required data. The remaining differences may arise due to several other factors that differ between the data sets, including the accelerating voltage (300 versus 200 kV), detector (film versus electronic detector), pixel size (1.23 Å versus 1.42 Å), grids (a combination of lacey carbon and C-flat versus solely C-flat), beam diameter, and stage drift rates; all of these factors preclude a fully quantitative comparison.

While motion tracking significantly enhances the data, the need for over half a million subunits to obtain an ~4 Å map still exceeds by at least an order of magnitude the number of particles that would be required based on calculations of the SNR of idealized low-dose images (Glaeser, 1999; Henderson, 1995). Several factors may contribute to this difference. The data in our study were collected on a nonbackthinned CMOS direct electron detector that has a detective quantum efficiency (DQE) inferior to that of photographic film at the resolution evaluated here (about 70% Nyquist frequency; McMullan et al., 2009). We thus expect the map quality to improve further when data are collected at 300 kV using backthinned CMOS chips that will be available with new direct electron detectors (McMullan et al., 2009). Furthermore, the motion tracking we have implemented may not completely compensate for the particle shifts, due to positional inaccuracy. The tracking of particle motion in our current work was done for individual particles, which provided sufficiently strong contrast due to the high molecular mass (70 MDa) of the particle. We showed in our earlier work (Brilot et al., 2012) that neighboring particles move together because the motion appears to be caused by the embedding ice layer moving as a whole. The positional tracking can therefore be made more accurate by imposing correlations between particles. This will be especially important when tracking particles with smaller mass that do not produce strong contrast. An interesting further improvement may be possible when imaging particles with lower molecular mass. Due to their weak low-resolution contrast, these particles are more prone to misalignment than particles with a high molecular mass (Henderson et al., 2011). The low-resolution contrast can be enhanced by using a higher dose, at the expense of the high-resolution signal, which fades more rapidly with dose than the low-resolution signal (Baker et al., 2010; Hayward and Glaeser, 1979). Using movies, the effective dose that contributes to a reconstruction can be adjusted by limiting the number of included frames. Thus, a dose-dependent frame filtering could be used to amplify both the low- and high-resolution contrasts. The traditional dose limit in low-dose cryo-EM must therefore be re-evaluated to find the optimum when using this new approach (Baker et al., 2010; Hayward and Glaeser, 1979).

An important result from our data is the reduction in the amount of observed particle rotations compared with our previous study (Brilot et al., 2012). There are two differences in the way the sample was illuminated by the beam. In the previous work, the beam was adjusted to a diameter of 2.0 μm to cover a variety of hole diameters, including the 1.6 μm holes found on Quantifoil grids. In the present study, the beam diameter was kept at

1.3 μm, covering less than half the area compared with the previous study. The reduction in BIM may thus be similar to that observed with the spot-scan technique (Bullough and Henderson, 1987), arising primarily from a smaller beam size. Second, while in the earlier work the area exposed to the electron beam included entire holes in the carbon support film, we limited the exposed area in our present work to include only one side of a hole. It is not yet clear how much of each of these differences is responsible for the reduced particle rotations. However, as our analysis shows, taking into account the particle rotations in the movie frame alignment has a fairly insignificant effect on the reconstructions. This indicates that particle rotations can be ignored in a simplified processing scheme, especially when dealing with smaller particles, for which a given rotational blur will have less of an impact as compared to larger particles.

The recording of movies also allows for compensation of stage and microscope instabilities. While exposure times have been traditionally limited to 1–2 s when working with side-entry stages to avoid blurring due to stage drift, the ability to record movies can reduce or eliminate this constraint. As a result, exposures can be longer, enabling the use of smaller condenser spot sizes and apertures so as to increase beam coherence, which, in turn, will enhance the high-resolution signal in the recorded images. The ability to record movies therefore represents a way to overcome limited mechanical stability and enhance beam coherence of midrange electron microscopes.

EXPERIMENTAL PROCEDURES

Electron Microscopy

Rotavirus DLPs were prepared as described (Street et al., 1982). Three microliters of sample with a concentration of 2.5 mg/ml were applied to a 1.2–1.3 C-flat grid, which had been glow discharged for 45 s at 20 mA. The grid was immediately plunge-frozen using an FEI Vitrobot Mark 2. The relative humidity was set at 85%, with 7 s blot time. Movies were collected at 25 frames per second on a DE-12 4k × 3k pixel direct electron detector (Direct Electron, San Diego, CA, USA) mounted on an FEI TF20 electron microscope operating at 200 kV, using a side-entry Gatan 626 cryo holder. Data collection was automated using *Leginon* (Suloway et al., 2005), which had been adapted to handle movies. The movies contained 18 frames, the first two of which were recorded with a blanked beam to ensure that the entire exposures were captured by the movies. These first two frames were excluded from subsequent processing, leaving 16 usable frames. The beam was adjusted to deliver a dose of about 2 electrons/$Å^2$ per frame, or a total dose of about 32 electrons/$Å^2$ over the duration of the movies. The relatively high dose rate of 50 electrons/$Å^2$/s was used to keep the total exposure time short, thereby minimizing stage instabilities as a source of the observed particle motions (see Results). However, as shown here, movie frame alignment compensates for both stage drift and BIM. In future experiments, it may therefore be more appropriate to use a lower dose rate (e.g., 25 electrons/$Å^2$/s) to increase beam coherence. Magnification adjustment was performed by maximizing the correlation coefficient between density derived from the DLP crystal structure (PDB ID: 3KZ4, McClain et al., 2010) and 3D reconstructions of DLP, giving a calibrated magnification of 42,135×. This corresponded to a pixel size on the specimen of 1.424 Å. Images were underfocused between 0.8 and 2.7 μm.

Movie Processing

We collected 561 movies of DLP samples and selected 1,915 particles from 501 movies after visual inspection, excluding micrographs that showed clear evidence of thick ice, contamination, or large sample drift. Particles were selected manually from images that were calculated by simple averaging of the frames. Simple frame averages were also used to determine image defocus using the computer program *CTFFIND3* (Mindell and Grigorieff, 2003), followed by further contrast transfer function correction with the computer program *FREALIGN* (Grigorieff, 2007) during refinement. The particle coordinates were then used to excise stacks of 16 frames with 800 × 800 pixel dimensions from the gain and dark-current corrected movies using computer program *label* from the MRC image processing suite (Crowther et al., 1996). These "particle" movies were used for further processing to track sample motion and calculate 3D reconstructions.

Euler angles as well as x and y coordinates of the excised DLPs were initially determined from the simple averages of the 16 movie frames and used for 3D reconstruction using *FREALIGN* (Grigorieff, 2007). Refinement of the reconstruction was performed as described (Chen et al., 2009) until there was no further improvement in the resolution. During the refinement, only data up to a resolution of 7.5 Å were used to avoid possible overfitting and bias in the FSC curves at higher resolution (Grigorieff, 2000; Stewart and Grigorieff, 2004). Based on the correlation coefficients calculated by *FREALIGN*, the best 42% (807) of the particles were selected for further processing. With respect to reconstructions using the full data set, the selection of this subset of the particles did not change the resolution of the reconstructions as measured by different FSC criteria (FSC = 0.5, Böttcher et al., 1997; FSC = 0.143, Rosenthal and Henderson, 2003). This result indicates that about 60% of the particles did not contribute significantly to the high-resolution signal in the reconstruction. A similar percentage of particle images (46%) was also selected from the 2008 data set of DLP (Zhang et al., 2008), thus ensuring similar conditions used in both cases for a more meaningful comparison of the final density maps in Figure 4. Thirteenfold nonicosahedral averaging was performed as described (Zhang et al., 2008), using the same symmetry matrices that were derived for the 2008 data set, again to maintain comparable conditions.

For the alignment of movie frames to compensate for sample motion, we developed two computer programs: *INTERPOLATE*, which calculated shifts for individual frames based on *FREALIGN* alignment parameters determined from frame averages, and *UNBLUR*, which applies the interpolated shifts to the movie frames. These programs are freely available from the Grigorieff lab Web page (http://emlab.rose2.brandeis.edu/).

ACCESSION NUMBERS

The Electron Microscopy Data Bank (EMDB) accession numbers for the uncorrected and motion-compensated 3D reconstructions of DLP and the 13-fold locally averaged VP6 trimer reported in this article are EMD-5485 (DLP, uncorrected), EMD-5486 (DLP, compensated for particle rotations and shifts), EMD-5487 (VP6, uncorrected), and EMD-5488 (VP6, compensated for particle rotations and shifts).

REFERENCES

Baker, L.A., Smith, E.A., Bueler, S.A., and Rubinstein, J.L. (2010). The resolution dependence of optimal exposures in liquid nitrogen temperature electron cryomicroscopy of catalase crystals. J. Struct. Biol. *169*, 431–437.

Böttcher, B., Wynne, S.A., and Crowther, R.A. (1997). Determination of the fold of the core protein of hepatitis B virus by electron cryomicroscopy. Nature *386*, 88–91.

Brilot, A.F., Chen, J.Z., Cheng, A., Pan, J., Harrison, S.C., Potter, C.S., Carragher, B., Henderson, R., and Grigorieff, N. (2012). Beam-induced motion of vitrified specimen on holey carbon film. J. Struct. Biol. *177*, 630–637.

Bullough, P., and Henderson, R. (1987). Use of spot-scan procedure for recording low-dose micrographs of beam-sensitive specimens. Ultramicroscopy *21*, 223–229.

Cambie, R., Downing, K.H., Typke, D., Glaeser, R.M., and Jin, J. (2007). Design of a microfabricated, two-electrode phase-contrast element suitable for electron microscopy. Ultramicroscopy *107*, 329–339.

Chen, J.Z., Settembre, E.C., Aoki, S.T., Zhang, X., Bellamy, A.R., Dormitzer, P.R., Harrison, S.C., and Grigorieff, N. (2009). Molecular interactions in rotavirus assembly and uncoating seen by high-resolution cryo-EM. Proc. Natl. Acad. Sci. USA *106*, 10644–10648.

Crowther, R.A., Henderson, R., and Smith, J.M. (1996). MRC image processing programs. J. Struct. Biol. *116*, 9–16.

Danev, R., and Nagayama, K. (2001). Transmission electron microscopy with Zernike phase plate. Ultramicroscopy *88*, 243–252.

Ermantraut, E., Wohlfart, K., and Tichelaar, W. (1998). Perforated support foils with pre-defined hole size, shape and arrangement. Ultramicroscopy *74*, 75–81.

Glaeser, R.M. (1999). Review: electron crystallography: present excitement, a nod to the past, anticipating the future. J. Struct. Biol. *128*, 3–14.

Goddard, T.D., Huang, C.C., and Ferrin, T.E. (2007). Visualizing density maps with UCSF Chimera. J. Struct. Biol. *157*, 281–287.

Grigorieff, N. (2000). Resolution measurement in structures derived from single particles. Acta Crystallogr. D Biol. Crystallogr. *56*, 1270–1277.

Grigorieff, N. (2007). FREALIGN: high-resolution refinement of single particle structures. J. Struct. Biol. *157*, 117–125.

Grigorieff, N., and Harrison, S.C. (2011). Near-atomic resolution reconstructions of icosahedral viruses from electron cryo-microscopy. Curr. Opin. Struct. Biol. *21*, 265–273.

Hayward, S.B., and Glaeser, R.M. (1979). Radiation damage of purple membrane at low temperature. Ultramicroscopy *04*, 201–210.

Henderson, R. (1995). The potential and limitations of neutrons, electrons and X-rays for atomic resolution microscopy of unstained biological molecules. Q. Rev. Biophys. *28*, 171–193.

Henderson, R., Baldwin, J.M., Ceska, T.A., Zemlin, F., Beckmann, E., and Downing, K.H. (1990). Model for the structure of bacteriorhodopsin based on high-resolution electron cryo-microscopy. J. Mol. Biol. *213*, 899–929.

Henderson, R., Chen, S., Chen, J.Z., Grigorieff, N., Passmore, L.A., Ciccarelli, L., Rubinstein, J.L., Crowther, R.A., Stewart, P.L., and Rosenthal, P.B. (2011). Tilt-pair analysis of images from a range of different specimens in single-particle electron cryomicroscopy. J. Mol. Biol. *413*, 1028–1046.

Jensen, G.J. (2001). Alignment error envelopes for single particle analysis. J. Struct. Biol. *133*, 143–155.

Kühlbrandt, W., Wang, D.N., and Fujiyoshi, Y. (1994). Atomic model of plant light-harvesting complex by electron crystallography. Nature *367*, 614–621.

Majorovits, E., Barton, B., Schultheiss, K., Pérez-Willard, F., Gerthsen, D., and Schröder, R.R. (2007). Optimizing phase contrast in transmission electron microscopy with an electrostatic (Boersch) phase plate. Ultramicroscopy *107*, 213–226.

McClain, B., Settembre, E., Temple, B.R., Bellamy, A.R., and Harrison, S.C. (2010). X-ray crystal structure of the rotavirus inner capsid particle at 3.8 Å resolution. J. Mol. Biol. *397*, 587–599.

McMullan, G., Chen, S., Henderson, R., and Faruqi, A.R. (2009). Detective quantum efficiency of electron area detectors in electron microscopy. Ultramicroscopy *109*, 1126–1143.

Milazzo, A.C., Leblanc, P., Duttweiler, F., Jin, L., Bouwer, J.C., Peltier, S., Ellisman, M., Bieser, F., Matis, H.S., Wieman, H., et al. (2005). Active pixel sensor array as a detector for electron microscopy. Ultramicroscopy *104*, 152–159.

Mindell, J.A., and Grigorieff, N. (2003). Accurate determination of local defocus and specimen tilt in electron microscopy. J. Struct. Biol. *142*, 334–347.

Muller, H., Jin, J., Danev, R., Spence, J., Padmore, H., and Glaeser, R.M. (2010). Design of an electron microscope phase plate using a focused continuous-wave laser. New J. Physics *12*, 073011. http://dx.doi.org/10.1088/1367-2630/12/7/073011.

Nogales, E., Wolf, S.G., and Downing, K.H. (1998). Structure of the alpha beta tubulin dimer by electron crystallography. Nature *391*, 199–203.

Penczek, P.A., Kimmel, M., and Spahn, C.M. (2011). Identifying conformational states of macromolecules by eigen-analysis of resampled cryo-EM images. Structure *19*, 1582–1590.

Quispe, J., Damiano, J., Mick, S.E., Nackashi, D.P., Fellmann, D., Ajero, T.G., Carragher, B., and Potter, C.S. (2007). An improved holey carbon film for cryo-electron microscopy. Microsc. Microanal. *13*, 365–371.

Rosenthal, P.B., and Henderson, R. (2003). Optimal determination of particle orientation, absolute hand, and contrast loss in single-particle electron cryomicroscopy. J. Mol. Biol. *333*, 721–745.

Sachse, C., Chen, J.Z., Coureux, P.D., Stroupe, M.E., Fändrich, M., and Grigorieff, N. (2007). High-resolution electron microscopy of helical specimens: a fresh look at tobacco mosaic virus. J. Mol. Biol. *371*, 812–835.

Scheres, S.H., Gao, H., Valle, M., Herman, G.T., Eggermont, P.P., Frank, J., and Carazo, J.M. (2007). Disentangling conformational states of macromolecules in 3D-EM through likelihood optimization. Nat. Methods *4*, 27–29.

Stewart, A., and Grigorieff, N. (2004). Noise bias in the refinement of structures derived from single particles. Ultramicroscopy *102*, 67–84.

Street, J.E., Croxson, M.C., Chadderton, W.F., and Bellamy, A.R. (1982). Sequence diversity of human rotavirus strains investigated by northern blot hybridization analysis. J. Virol. *43*, 369–378.

Suloway, C., Pulokas, J., Fellmann, D., Cheng, A., Guerra, F., Quispe, J., Stagg, S., Potter, C.S., and Carragher, B. (2005). Automated molecular microscopy: the new Leginon system. J. Struct. Biol. *151*, 41–60.

Tang, G., Peng, L., Baldwin, P.R., Mann, D.S., Jiang, W., Rees, I., and Ludtke, S.J. (2007). EMAN2: an extensible image processing suite for electron microscopy. J. Struct. Biol. *157*, 38–46.

Thon, F. (1966). Zur Defokussierungsabhängigkeit des Phasenkontrastes bei der elektronenmikroskopischen Abbildung [Defocus dependence of the phase contrast in the electron microscopic image]. Zeitschrift für Naturforschung *21a*, 476–478.

Unwin, N. (2005). Refined structure of the nicotinic acetylcholine receptor at 4Å resolution. J. Mol. Biol. *346*, 967–989.

Yonekura, K., Maki-Yonekura, S., and Namba, K. (2003). Complete atomic model of the bacterial flagellar filament by electron cryomicroscopy. Nature *424*, 643–650.

Zhang, X., Settembre, E., Xu, C., Dormitzer, P.R., Bellamy, R., Harrison, S.C., and Grigorieff, N. (2008). Near-atomic resolution using electron cryomicroscopy and single-particle reconstruction. Proc. Natl. Acad. Sci. USA *105*, 1867–1872.